Magnetic and dielectric response in yttrium (Y)-manganese (Mn) substituted multiferroic $Bi_{1-x}Y_xFe_{1-y}Mn_yO_3$ ($x = y = 0$; $x = 0.03, 0.06, 0.12$, $y = 0.05$) ceramics

A. K. Jena, S. Satapathy, and J. Mohanty

Citation: Journal of Applied Physics **124**, 174103 (2018); doi: 10.1063/1.5039620
View online: https://doi.org/10.1063/1.5039620
View Table of Contents: http://aip.scitation.org/toc/jap/124/17
Published by the American Institute of Physics

Magnetic and dielectric response in yttrium (Y)-manganese (Mn) substituted multiferroic $Bi_{1-x}Y_xFe_{1-y}Mn_yO_3$ ($x = y = 0$; $x = 0.03, 0.06, 0.12$, $y = 0.05$) ceramics

A. K. Jena,[1] S. Satapathy,[2,3] and J. Mohanty[1,a)]
[1]*Nanomagnetism and Microscopy Laboratory, Department of Physics, Indian Institute of Technology Hyderabad, Kandi, Sangareddy 502285, Telangana, India*
[2]*Laser Material Section, Raja Ramanna Center for Advanced Technology, Indore 452013, India*
[3]*Homi Bhaba National Institute, Training School Complex, Anushakti Nagar, Mumbai 40094, India*

(Received 9 May 2018; accepted 14 October 2018; published online 2 November 2018)

The effect of Y and Mn substitution on the structural, magnetic, and dielectric properties of $Bi_{1-x}Y_xFe_{1-y}Mn_yO_3$ ($x = y = 0$; $x = 0.03, 0.06, 0.12$, $y = 0.05$) is investigated. X-ray diffraction and Raman spectroscopy analysis revealed that all the compounds were stabilized in the Rhombohedral structure (Space group: R3c) below Y(6%)-Mn co-doping. A minimal contribution from the Pbam phase was also observed at higher Y (12%). Co-doped compounds exhibit canted ferromagnetic behavior with a significant increase in the saturation magnetization (M_s) of 1.28 emu/g when (Y, Mn)= (0.12, 0.05). Dielectric measurements at different temperatures ranging between 30 °C and 210 °C in a wide frequency range of 1 Hz–1 MHz were investigated. Impedance study is useful to understand the correlation of grain and grain boundary with electrical properties. The grain and grain boundary contribution to electrical parameters was presented with equivalent R-C circuit. Furthermore, electrical properties such as complex electrical modulus and electrical conductivity analysis clearly emphasize the substitution of Y and Mn, leading to a significant change in $BiFeO_3$ ceramic. *Published by AIP Publishing.* https://doi.org/10.1063/1.5039620

I. INTRODUCTION

Multiferroic materials are materials that combine two or more of the primary forms of ferroic order, i.e., ferromagnetic, ferroelectric, ferroelastic, etc., and are focused on more in previous years due to their tremendous applications in non-volatile memory devices, sensors, and actuators.[1–4] Bismuth ferrite ($BiFeO_3$) is one of the most studied and promising multiferroic materials to date, having the rhombohedral distorted structure with an R3c space group. Stable structure and properties well above room temperature (high Curie temperature $T_c = 1103$ K and Néel temperature $T_n = 643$ K) make $BiFeO_3$ as a potential candidate for novel applications.[5] The presence of magneto-electric coupling in these materials is highly useful in understanding the magnon and phonon behavior in Tera-hertz region[6] and cancer cell drug delivery.[7] The synthesis of single phase $BiFeO_3$ (BFO) is difficult in the conventional solid state synthesis due to Bi-loss at a high sintering temperature. Furthermore, perturbations such as high leakage current, spiral spin modulated structure (SSMS) hinder the electric and magnetic properties of this material. Methods such as doping and co-doping are highly useful to achieve single phase formation of the material. Other alternative methods are rapid thermal annealing, quenching, or making thin films. Previous reports suggest that the multiferroic properties of $BiFeO_3$ (BFO) improve significantly either by doping with rare earth magnetic element (Ho^{3+}, Eu^{3+}, Gd^{3+})[8–10] and transition metal elements (Mn^{3+}, Co^{3+}, Sc^{3+})[11–13] or co-doping with (Nd, Gd), (Nd, Sc), (Y, Zr), etc.[14–16]

In the present work, we report a brief discussion on the structural, magnetic, and dielectric properties of Y-Mn co-doped $Bi_{1-x}Y_xFe_{1-y}Mn_yO_3$ ($x = y = 0$; $x = 0.03$, 0.06, 0.12, $y = 0.05$) compounds. The formation of a novel single phase BFO (below 6% Y with Mn 5%), significant enhancement in the magnetic properties, and contribution of grain and grain boundaries to electrical properties are major highlights in this system.

II. EXPERIMENTAL PROCEDURE

Multiferroic $Bi_{1-x}Y_xFe_{1-y}Mn_yO_3$ [$x = y = 0$ (BFO); $x = 0.03$ (BY3FMO), 0.06 (BY6FMO), 0.12 (BY12FMO), $y = 0.05$] ceramics were synthesized by the conventional solid state reaction method using the high energy ball milling technique. High purity Bi_2O_3, Y_2O_3, Fe_2O_3, Mn_2O_3 powders were taken in a stoichiometric ratio in toluene medium and ground for 16 h. The details of the synthesis process are reported elsewhere.[17]

The crystalline structure and phase analysis were carried out by the X-ray diffraction (XRD) technique (PanAnalytic Pro) with Cu-Kα ($\lambda = 1.54\,A^0$). Grain size distribution and microstructural analysis were performed with the field effect scanning electron microscope (FESEM). Room temperature magnetic hysteresis (M-H) measurements were taken using a vibrating sample magnetometer (VSM) with the maximum field of 1.5 T (ADE Technologies USA, EV7 VSM). Magnetization-temperature (M-T) measurement was performed on all samples between the temperature range of 300 and 800 K at a field of 1000 Oe. Frequency dependent dielectric measurements were carried out on silver coated pellets at

a)Electronic mail: jmohanty@iith.ac.in

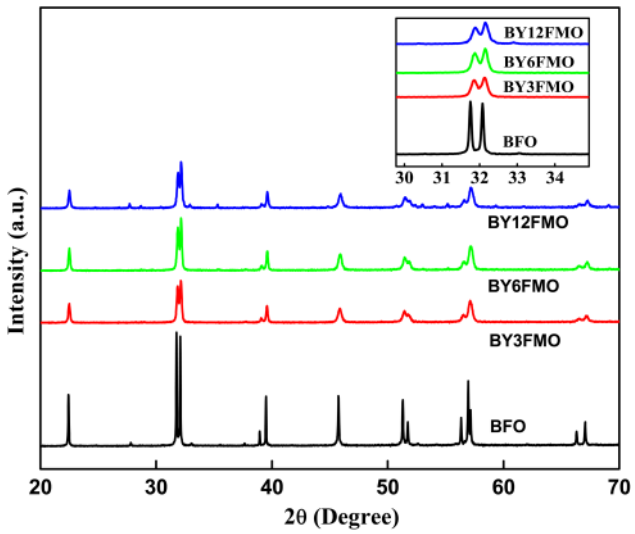

FIG. 1. Room temperature XRD pattern for Y and Mn co-doped $Bi_{1-x}Y_xFe_{1-y}Mn_yO_3$ ($x = y = 0$; $x = 0.03, 0.06, 0.12$, $y = 0.05$).

different temperatures ranging from 30 °C to 210 °C in the frequency range of 1 Hz − 1 MHz.

III. STRUCTURAL ANALYSIS

Figure 1 shows sharp and well defined good crystallinity XRD patterns of polycrystalline BFO, BY3FSO, BY6FMO, and BY12FMO compounds. All the major peaks are well matched with the rhombohedral R3c structure (JCPDS 71-2494). Traces of $Bi_2Fe_4O_9$ impurity peaks are appearing for (Y, Mn) = (6%, 5%), which usually comes with BFO.[18] At higher Y-concentration (BY12FMO), the percentage of impurity phase $Bi_2Fe_4O_9$ is increased with the appearance of additional traces of impurity $Bi_{25}FeO_{39}$.[19] The inset of Fig. 1 shows slight displacement of major peaks toward higher Bragg angle confirming structural distortion due to ionic radii difference between Fe^{3+} ($0.645\,A^0$) and Mn^{3+}($0.785\,A^0$). To confirm the structural distortion and phase purity, Rietveld refinement was carried out for all samples, which is shown in Fig. 2.

Rietveld refinement plots for BFO and co-doped compounds are shown in Fig. 2. All the compounds are well fitted with the rhombohedral R3c structure with lower χ^2 value. Furthermore, the evolution of other phases ($Bi_2Fe_4O_9$, $Bi_{25}FeO_{39}$) in BY12FMO compound is also evident from Fig. 2. After rigorous fitting with several phases, we obtained best fit with orthorhombic Pbam phase [R3c(86%)+ Pbam(14%)]. The structural parameters extracted from the refinement are shown in Table I. The extracted oxygen positions for orthorhombic Pbam phase in BY12FMO are (x, y, z) = O1 (0.259, 0.169, 0), O2 (0.273, 0.077, 0.5), O3 (0.008, 0.242, 0.291), O4 (0, 5, 0.203), O5 (0, 0, 0.205). The change in lattice parameters (a, b, and c), the volume of unit cell (V), bond length (Bi-O, Fe-O), and bond angle (Fe-O-Fe) confirms the structural distortion. These changes may create internal chemical pressure and FeO_6 octahedral distortion.

Room temperature Lorentzian-fitted Raman spectra for BFO and Y-Mn co-doped BFO are shown in Fig. 3. The positions of each mode extracted from fitting results are given in Table II. According to the group theory and from other experimental results, there should be 13 possible spectra for BFO, assigned by the equation[20,21]

$$\gamma = 4A1 + 9E, \tag{1}$$

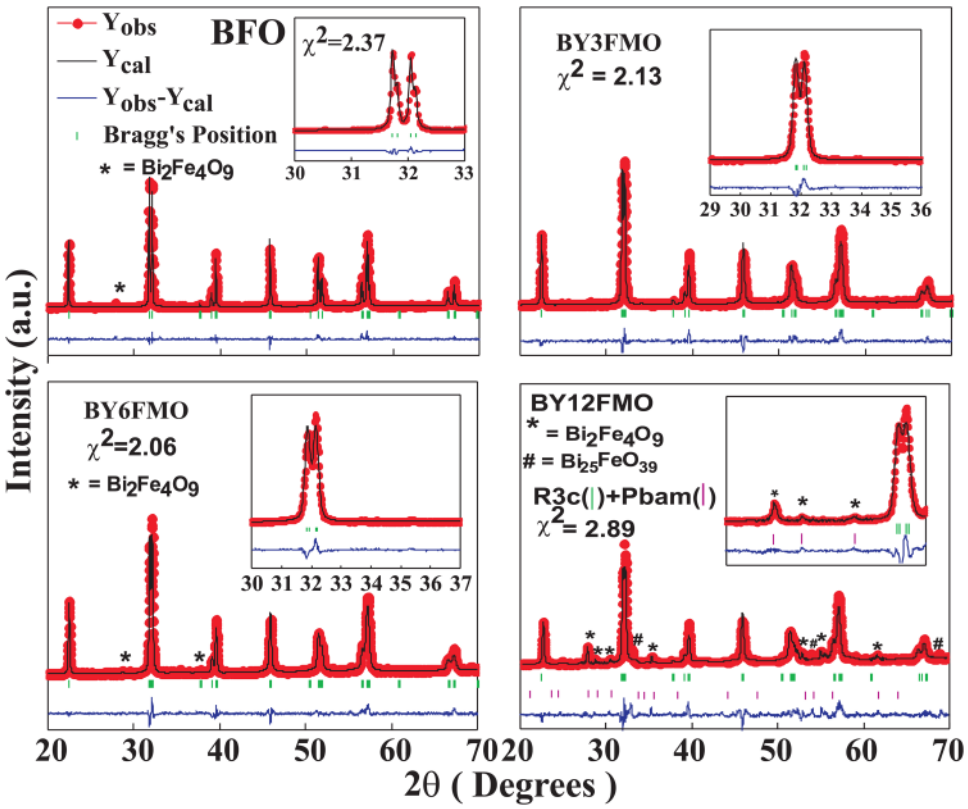

FIG. 2. Reitvield refinement of BFO, BY3FMO, BY6FMO, and BY12FMO.

TABLE I. Structural parameters of Y-Mn co-doped $Bi_{1-x}Y_xFe_{1-y}Mn_yO_3$ ($x = y = 0$; $x = 0.03, 0.06, 0.12$, $y = 0.05$).

Sample code		BFO	BY3FMO	BY6FMO	BY12FMO R3c (86%)	Pbam (14%)
a = b(A^0)		5.5802(2)	5.5722(6)	5.5683(3)	5.5687(2)	a = 5.6125(6), b = 11.2436(3)
c(A^0)		13.8727(7)	13.5254(4)	13.8171(2)	13.8201(9)	7.8120(9)
Volume(A^{0^3})		374.10(8)	371.75(3)	371.01(8)	371.16(7)	493.24(6)
Bi/Y	x	0	0	0	0	0.739(11)
	y	0	0	0	0	0.1364(5)
	z	0	0	0	0	0
Fe/Mn	x	0	0	0	0	0.2324
	y	0	0	0	0	0.1239
	z	0.2190	0.2218	0.2208	0.2226	0.2451
O	x	0.4540	0.4318	0.5378	0.454	
	y	0.0088	0.0125	0.0113	0.018	
	z	0.9575	0.9572	0.9638	0.9564	
Fe-O		1.951(7)	1.96(6)	1.97(3)	1.96(11)	1.93(3)
Bi-O1		2.57(11)	2.44(8)	2.65(5)	2.51(4)	1.98(4)
Bi-O2		2.346(9)	2.345(8)	2.336(4)	2.321(4)	2.117(4)
Fe-O-Fe		161.60(4)	163.76(4)	167.85(9)	158.6(8)	151.8(2)
χ^2		2.37	2.13	2.06	2.89	

where A-Modes at low-frequency region are due to parallel polarization and E-Modes at the high-frequency region are due to cross polarization.[24] In our system, for parent BFO, there exist 12 phonon modes, whereas for the Y-Mn co-doped system, there are 11 phonon modes as evident from Fig. 3. Raman spectra corresponding to A-mode and E-modes are assigned to Bi-O bonds (below 400 cm^{-1}) and Fe-O bonds (above 400 cm^{-1}), respectively. Furthermore, shifting of phonon modes was also observed from Table II with the increase in Y-concentration at a constant Mn concentration. The shifting of modes confirms distorted BFO structure as a result of the substitution of Y-Mn. With the increase in Y-concentration, the intensity of A-modes decreases, which may be due to the change in the Bi-O bond length and decline in stereochemical activity of $6s^2$ lone pair electron of Bi^{3+}, resulting in the change in the ferroelectric order.[22] Broadening of A-Modes is observed with the increase in Y-concentration (increase FWHM), due to the decrease in the lifetime of phonons in crystals (which is inversely proportional to the FWHM).[23] An extra weak Raman mode is observed between E8 and E9, which may arise from iron-rich impurity $Bi_2Fe_4O_9$.[25] From the above discussion, it is concluded that Y-Mn co-doping distorts the structure, which is well supported by XRD analysis.

Figure 4 shows FESEM micrographs of BFO, BY3FMO, BY6FMO, and BY12FMO at room temperature. For polycrystalline BFO, the grains are in the range of 6 μm constraint with well-defined boundary, whereas for the Y-Mn co-doped system, inhomogeneity in the grain size is observed. The average grain size of BY3FMO, BY6FMO, and BY12FMO is 2.1 μm, 1.7 μm, and 1.4 μm, respectively (with some voids created between loosely connected grains). The bond dissociation energy of Y-O bond (715 kJ/mol) is more than double the bond dissociation energy of Bi-O (339 kJ/mol). Hence, the Y substitution at Bi-site restricts the bismuth volatilization, lowers the oxygen vacancies,[26] and makes BFO thermally stable at the high sintering temperature which can be clearly seen in FESEM micrographs. The effect from Mn has less possibility due to almost similar bond dissociation energy of Fe-O (409 kJ/mol) and Mn-O (402 kJ/mol). The decrease in the grain size may be due to the ionic radii difference between Y^{3+} and Bi^{3+}, the variation of bond strength, and a lower diffusivity rate of Y^{3+}. The observation of secondary phases (observed from XRD) also appears in an agglomerate form.

IV. MAGNETIC PROPERTIES

Room temperature magnetic properties of BFO and Y-Mn co-doped BFO were studied with the maximum applied field of 15 kOe (shown in Fig. 5). The rhombohedral R3c BFO shows linear M-H loop confirming antiferromagnetic behavior. But due to Dzyaloshinskii-Moriya (DM) exchange interaction, a weak ferromagnetic behavior is observed due to spiral spin modulated structure (SSMS) below 62 nm. With co-doping of Y and Mn, the magnetization increases and complete saturation is observed in BY12FMO ceramic. The magnetic parameters are shown in Table III.

The saturation magnetization (M_s) is enhanced with the increase in Y-concentration at a constant Mn-concentration. The enhancement in magnetization with Y-Mn co-doped BFO system can be explained on the basis of magnetic interactions between the ions, FeO_6 octahedral distortion, and reduction in the grain size. It is reported that the observation of enhanced and saturated magnetization in BFO is possible with non-magnetic and stable element Y and Sc co-doping.[17] In the present work, the observation of well improved canted ferromagnetic behavior in the Y-Mn co-doped modified BFO system with saturation magnetization (M_s) is noticed. The enhanced magnetic properties can be believed due to the increase in super-exchange interaction between $Fe^{3+} - O^{2-} - Fe^{3+}$. The foreign paramagnetic dopant Mn_2O_3 oxide has +3 oxidation state. So, there is a

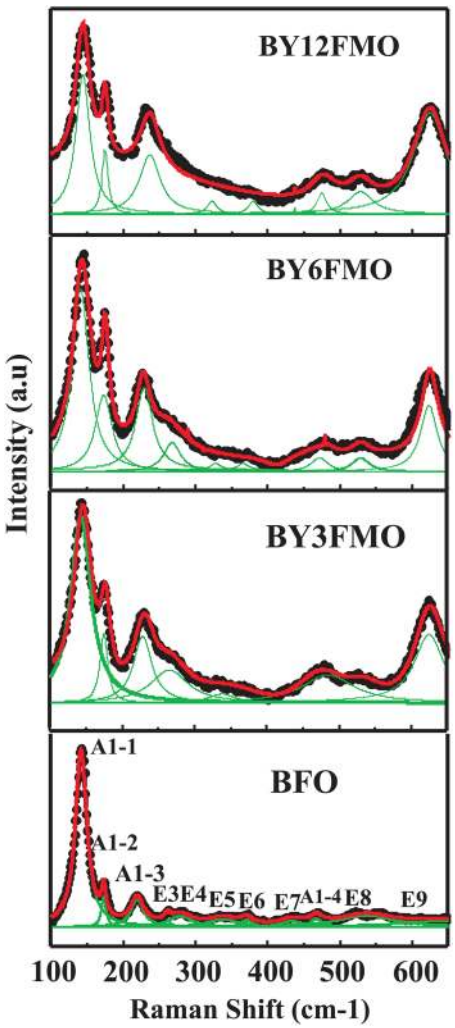

FIG. 3. Room temperature Raman active modes of un-doped and co-doped $Bi_{1-x}Y_xFe_{1-y}Mn_yO_3$ ($x = y = 0$; $x = 0.03, 0.06, 0.12$, $y = 0.05$).

possibility of the super-exchange interaction between $Fe^{3+} - O^{2-} - Mn^{3+}$. Furthermore, substituting Mn to Fe-site affects the local environment of FeO_6 octahedral due to the change in the Fe-O-Fe bond angle, which suppresses the spiral spin structure and/or improves the canting angle of antiferromagnetically ordered adjacent planes, resulting in

TABLE II. Raman vibrational modes of un-doped and co-doped $Bi_{1-x}Y_xFe_{1-y}Mn_yO_3$ ($x = y = 0$; $x = 0.03, 0.06, 0.12$, $y = 0.05$) samples.

Raman modes	BFO	BY3FMO	BY6FMO	BY12FMO
A1-1	140	143	144	145
A1-2	171	174	175	176
A1-3	219	226	227	229
E3	263	263	266	...
E4	282	309	312	323
E5	351	...	...	...
E6	367	371	375	376
E7	430	437	441	447
A1-4	469	476	478	481
E8	561	571	571	576
E9	607	619	623	625

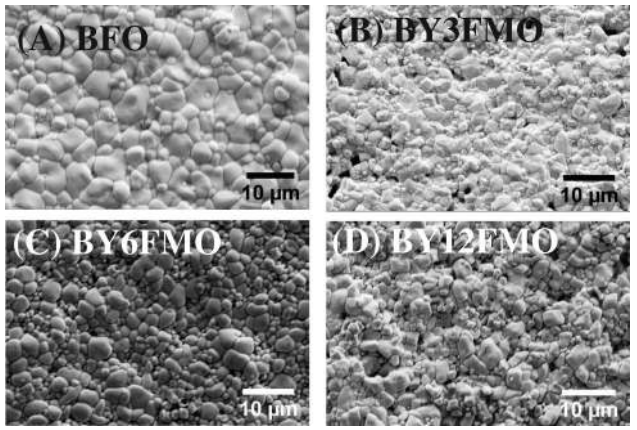

FIG. 4. FESEM imaging of un-doped and co-doped $Bi_{1-x}Y_xFe_{1-y}Mn_yO_3$ ($x = y = 0$; $x = 0.03, 0.06, 0.12$, $y = 0.05$).

improved ferromagnetism.[15] Again, a significant trace of impurities $Bi_2Fe_4O_9$ (14%) and a very small percentage $Bi_{25}FeO_{39}$ are observed for BY12FMO, which have no effect on magnetization due to its paramagnetic nature.[27] Also, there exists no magnetic interaction among Y, Bi, and O. In conclusion, the enhancement of magnetization is believed to be due to FeO_6 octahedral, suppressing SSMS and super-exchange interaction between Fe^{3+} and Mn^{3+} ions. Wen *et al.* reported that co-doping of Ba^{2+} and Mn^{3+} enhances magnetization due to double exchange interaction between Mn^{4+} and Fe^{2+}. But in our work, the chances of formation of Mn^{4+} are less and Mn is only available in +3 state.[28] So the possibility of double exchange interaction in our system can be ruled out. Also, the decrease in the grain size may enhance the magnetic properties. The decrease in the coercive field (H_c) from the vicinity of BFO is observed due to

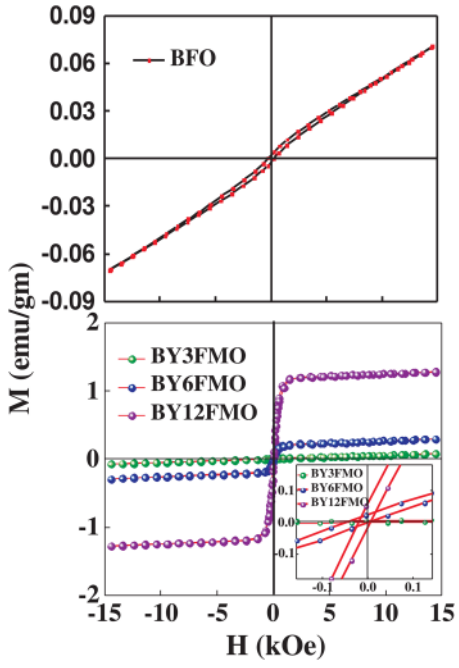

FIG. 5. Room temperature M-H measurements of Y-Mn co-doped $Bi_{1-x}Y_xFe_{1-y}Mn_yO_3$ ($x = y = 0$; $x = 0.03, 0.06, 0.12$, $y = 0.05$) samples.

TABLE III. Magnetization parameters of Y-Mn co-doped $Bi_{1-x}Y_xFe_{1-y}Mn_yO_3$ ($x = y = 0$; $x = 0.03, 0.06, 0.12$, $y = 0.05$) samples.

Sample code	M_r (emu/g)	M_s (emu/g)	H_c (kOe)
BFO	0.0028	0.070	0.266
BY3FMO	0.0032	0.07	0.207
BY6FMO	0.0201	0.30	0.036
BY12FMO	0.0635	1.28	0.017

the decrease in the anisotropy energy. The enhanced magnetic properties with the low value of the coercive field are useful for transformer and microwave applications.

Figure 6 shows the magnetization vs. temperature (M-T) plots for BFO, BY3FMO, BY6FMO, and BY12FMO compounds at a magnetic field of 1000 Oe in the temperature range of 300–800 K. Parent BFO shows the transition temperature (T_n) at 641 K, which represents the antiferromagnetic (AFM)–paramagnetic (PM) transition and the observed T_n is consistent with other reports.[15] With Y-Mn co-doping, minimal reduction of T_n is observed with the increase in Y-concentration. This may be due to the non-magnetic and stable nature of Y^{3+} ions, which do not take part in any magnetic interactions. Minimal reduction in T_n is also observed in different rare earth element dopings.[29] The decrease in T_n in the Y-Mn co-doped BFO system may be due to decreases in magnetic interaction and the presence of higher radii Mn^{3+} foreign element at Fe-site. Non-existence of other magnetic transitions helps us to believe that the enhancement in magnetization is possibly due to the unlocking of the SSMS and change in the bond length and bond angle.

V. DIELECTRIC PROPERTIES

Frequency dependence dielectric constant (ϵ_r) for un-doped BFO and Y-doped BFMO at different temperatures ranging from 30 °C to 210 °C is shown in Fig. 7. The ϵ_r value decreases with increase in frequency and attains saturation at higher frequency. At the very low frequency region, ϵ_r value is very high due to interfacial polarization (or Maxwell-Wagner type polarization),[30] where easy orientation of space charges is possible at the grain boundaries. The other polarizations, such as dipolar, ionic, and electronic polarization, play a role in improving dielectric constant (ϵ_r). As frequency increases up to 1 kHz, the effect from ionic and electronic polarization is less and dipolar polarization is the major contributor to ϵ_r. At the high frequency region, the dipoles do not match the applied field and result in reduced dielectric constant.[31] At the low frequency region, ϵ_r increases with increase in temperature due to increases in oxygen vacancy. This, in turn, confirms that the dipoles are thermally activated. The motion of these oxygen vacancies increases the conductivity, which increases the charge accumulation at grain boundaries due to defect polarization.

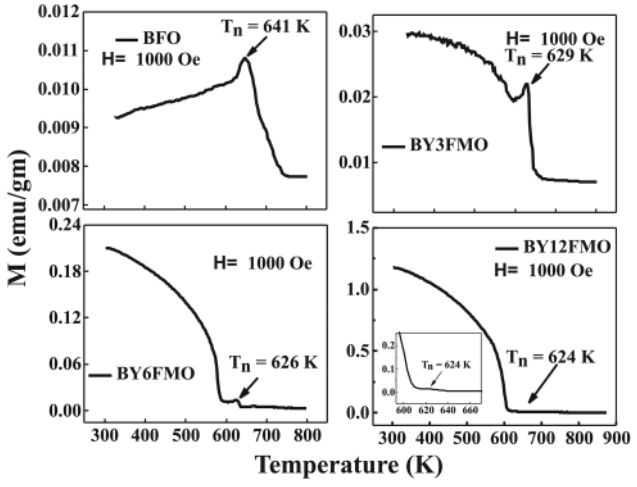

FIG. 6. M-T measurements for BFO, BY3FMO, BY6FMO, and BY12FMO.

Insets in Fig. 7 show the frequency dependence dielectric loss ($\tan\delta$) at different temperatures. For all samples, we observe a relaxation peak between the frequency range 10 kHz and 100 kHz, which is possibly due to the relaxation of defect charge carriers. The shifting of ($\tan\delta$) peak with increase in temperature confirms that the relaxation process is affected by thermal energy. By taking into account the equation

$$\omega\tau = 1, \tag{2}$$

the vibration of dipoles is faster at higher temperature, which needs very less time to align with the applied field confirming the shifting of relaxation peak toward higher frequency. The dielectric loss values at higher temperature are above unity, which may be due to the increase in oxygen vacancies.[9]

VI. IMPEDANCE SPECTROSCOPY

Impedance spectroscopy analysis (Z'/ Z'' vs frequency) is a powerful approach to relate grain and grain boundaries to electrical properties. The frequency and temperature dependence of complex impedance can be well explained in terms of the following equation:[9]

$$Z^* = Z_0(T)\int \frac{y(\tau, T)d(\tau)}{1 + j\omega\tau}. \tag{3}$$

Real and imaginary parts of complex impedance can be extracted from the above equation,

$$Z' = Z_0(T)\int \frac{y(\tau, T)d(\tau)}{1 + \omega^2\tau^2}, \tag{4}$$

$$Z'' = Z_0(T)\int \frac{(\omega\tau)^* y(\tau, T)d(\tau)}{1 + \omega^2\tau^2}, \tag{5}$$

where ω, τ, and $y(\omega, \tau)$ are the angular frequency, relaxation time, and relaxation time distributions, respectively.

Frequency dependence for the real part of complex impedance of BFO and Y-Mn co-doped BFO at various temperatures is shown in Figs. 8(a)–8(d). The observation of dispersion of Z' at the low-frequency region confirms the presence of dielectric relaxation in the studied system and it decreases with increase in frequency due to the defect charges that are not responding to these frequencies (shown

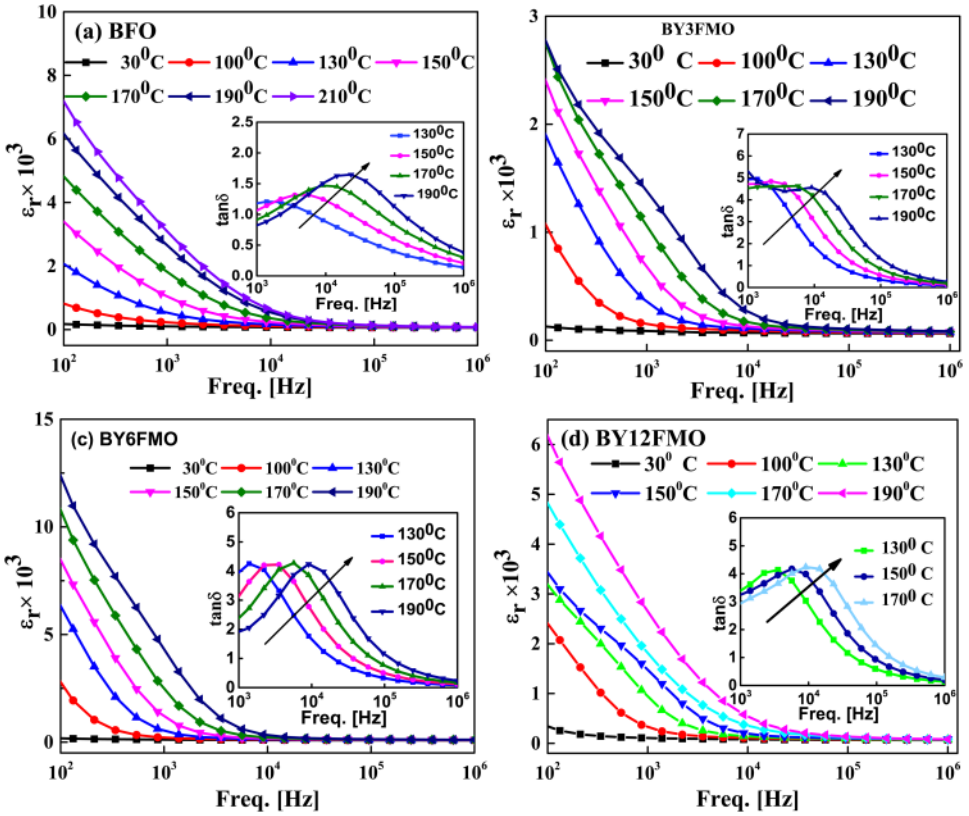

FIG. 7. Frequency dependence dielectric constant (ϵ_r) and dielectric loss ($\tan\delta$) measurements of un-doped and co-doped $Bi_{1-x}Y_xFe_{1-y}Mn_yO_3$($x = y = 0$; $x = 0.03, 0.06, 0.12$, $y = 0.05$).

in Fig. 11). As all the samples behave as a semiconducting material (bandgap range $E_g = 2.08$–2.18 eV), the decrements in the magnitude of Z′ with the increase in temperature can be expected due to negative temperature coefficient resistance (NTCR) effect. Again, with the increase in Y-concentration, the magnitude of Z′ increases for 3% and 6% due to improved bulk resistance.[34]

Figures 8(e)–8(h) show the frequency dependence imaginary part of complex impedance (Z″) at different temperatures of BFO and Y-Mn co-doped BFO system. The conduction mechanism of Y-Mn co-doped BFO system shows different behavior from BFO. In BFO above 150 °C, the Z″ shows dispersion behavior, while for other co-doped systems, two peaks are observed in the various frequency ranges 10^2 Hz–10^3 Hz and 10^4 Hz–10^5 Hz, confirming the presence of electrical relaxation in co-doped compounds. The observed peaks originated due to defect charge carriers. The peak at the low-frequency region is contributed by the

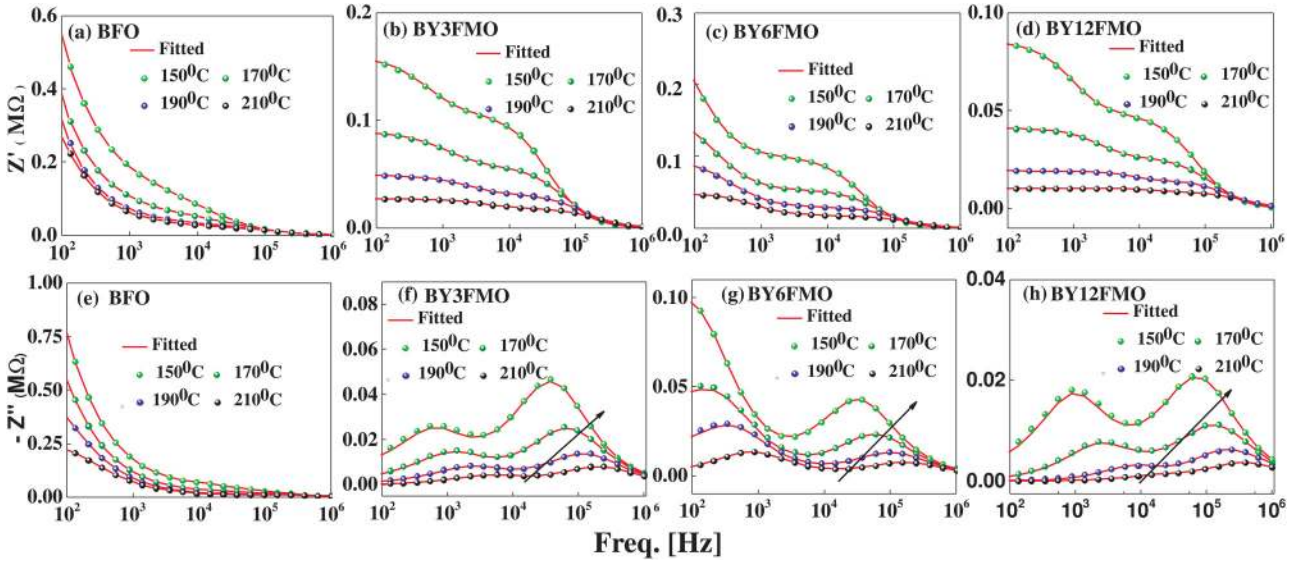

FIG. 8. Frequency dependence impedance spectroscopy for real part (Z′) for (a) BFO, (b) BY3FMO, (c) BY6FMO, (d) BY12FMO and imaginary part (Z″) for (e) BFO, (f) BY3FMO, (g) BY6FMO, (h) BY12FMO at different temperatures.

grain boundary and peak observed at the higher frequency region is contributed due to grains.[32] The origin of peaks may be due to unequal ionic radii of the parent (Bi^{3+}, Fe^{3+}) and foreign ions (Y^{3+}, Mn^{3+}), which creates defects such as oxygen vacancies in addition to charge carriers. With the increase in temperature, the shifting of relaxation peaks confirms that the Z″ depends on the thermal energy which gives additional energy to the electric field. Asymmetric broadening confirms the distribution of relaxation time (decrease in the relaxation time period).[9]

From FESEM micrograph, the inhomogeneous grain's structure with well separated grain boundaries confirms the polycrystallinity of the ceramics. The behavior of grain and grain boundary with electrical properties is well described by using Nyquist plots [shown in Fig. 9 for different temperatures (150 °C–210 °C)]. In the figure, we observe two semicircle arcs, one is at the lower frequency region contributed from grain boundaries and the other at the higher frequency region contributed from grains which is consistent with the "brick-layer model."[36] These semicircle arcs can be modeled in terms of equivalent electric circuits which are the series combination of two R-C circuits, where resistor (R) is connected parallel to the capacitor (C) or a constant phase element (CPE) as shown in the inset of Fig. 9. The impedance of the resultant circuit contributed from grains and grain boundaries can be expressed as[33]

$$z* = \frac{R_g}{1 + (j\omega R_g C_g)^{n_g}} + \frac{R_{gb}}{1 + (j\omega R_{gb} C_{gb})^{n_{gb}}}, \tag{6}$$

where R_g and R_{gb} are the resistances, C_g and C_{gb} are the capacitances, and n_g and n_{gb} are the relaxation time variables contributed from grain and grain boundaries, respectively. For an ideal ferroelectric material, the value of n should be one[35] and its value can be measured by its deviation from unity.

With the increase in temperature, the circular arcs compress and shift toward the origin as shown in Nyquist plots. This confirms that the R_g and R_{gb} values are decreasing in correspondence to the NTCR effect. The value of R_g and R_{gb} is obtained from fitting equivalent circuit. The R_g and R_{gb} values are found to be 0.025 MΩ and 0.05 MΩ for BFO, 0.1 MΩ and 0.084 MΩ for BY3FMO, 0.15 MΩ and 0.10 MΩ for BY6FMO, and 0.043 MΩ and 0.049 MΩ for BY12FMO. It is observed that the grain and grain boundary resistance increases up to 6% Y-concentration and again starts decreasing for higher (12%) Y-concentration due to the breakdown of the inhomogeneity of grain and pilling effect at the boundary. The substitution of Y^{3+} and Mn^{3+} to BFO improved the barrier properties through which the space charges are flown.[9]

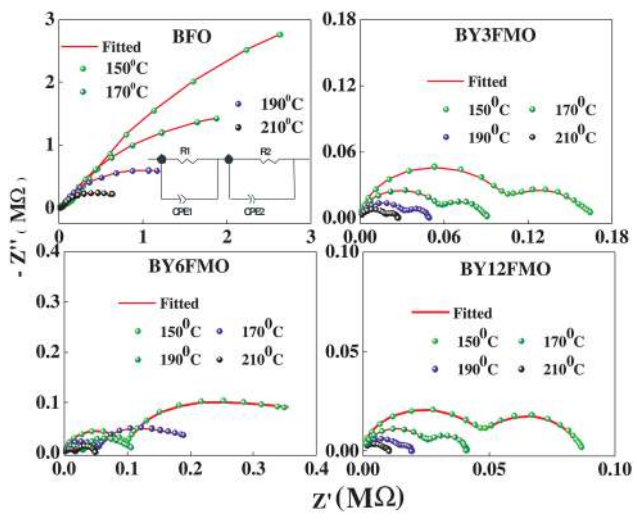

FIG. 9. Nyquist plots at different temperatures for BFO, BY3FMO, BY6FMO, and BY12FMO.

VII. COMPLEX ELECTRICAL MODULUS ANALYSIS

Electrical modulus study is a powerful tool to investigate the electrical response of the material and it behaves exactly in the opposite way to dielectric constant (ϵ_r), i.e., the magnitude is saturated at low-frequency and higher at the high-frequency region. In the modulus calculation, the intensity of relaxation peaks is inversely proportional to the capacitance of the material. As we have already seen in impedance spectroscopy, where C_{gb} dominated over C_g, the grain boundary capacitance plays a crucial role in the modulus study.

Mathematically complex modulus (M^*) spectra can be expressed as

$$\begin{aligned} M^* &= M' + M'' = i\omega C_0 Z^* = i\omega C_0 (Z' - iZ'') \\ &= \omega C_0 Z'' + i\omega C_0 Z', \end{aligned} \tag{7}$$

where ω is the frequency of the applied electric field and C_0 is the capacitance in the vacuum. Figures 10(a)–10(d) show the frequency dependency of the real part of the electrical modulus (M′) at different temperatures for un-doped BFO and Y-Mn co-doped BFO. At the low-frequency region, the value of M′ is very low, approximately close to zero due to high capacitive nature of the material and showing dispersion behavior with the increase in frequency. The magnitude of M′ is minimal from the low- to high-frequency region, suggesting negligible electrode polarization phenomenon in the test materials.[37]

It is also observed that with the increase in temperature the dispersion region shifts toward the high-frequency region, confirming that the polarization is thermally activated. The magnitude of M′ decreases with increase in temperature which is also confirmed from the dielectric analysis. The dielectric constant increases with increase in temperature due to extra thermal energy provided to the external field, i.e., capacitance also increases from the relation

$$C = \frac{\epsilon A}{d}, \tag{8}$$

where C is the capacitance, A is the area, and d is the thickness of the sample. Hence, decrease in the electrical modulus is expected.

Frequency dependence of the imaginary part (M″) of the complex electrical modulus at different temperatures for BFO and Y-Mn co-doped BFO is shown in Figs. 10(e)–10(h). The value of M'' is minimal at the low-frequency region and increases to M''_{max} and again decreases with further increase

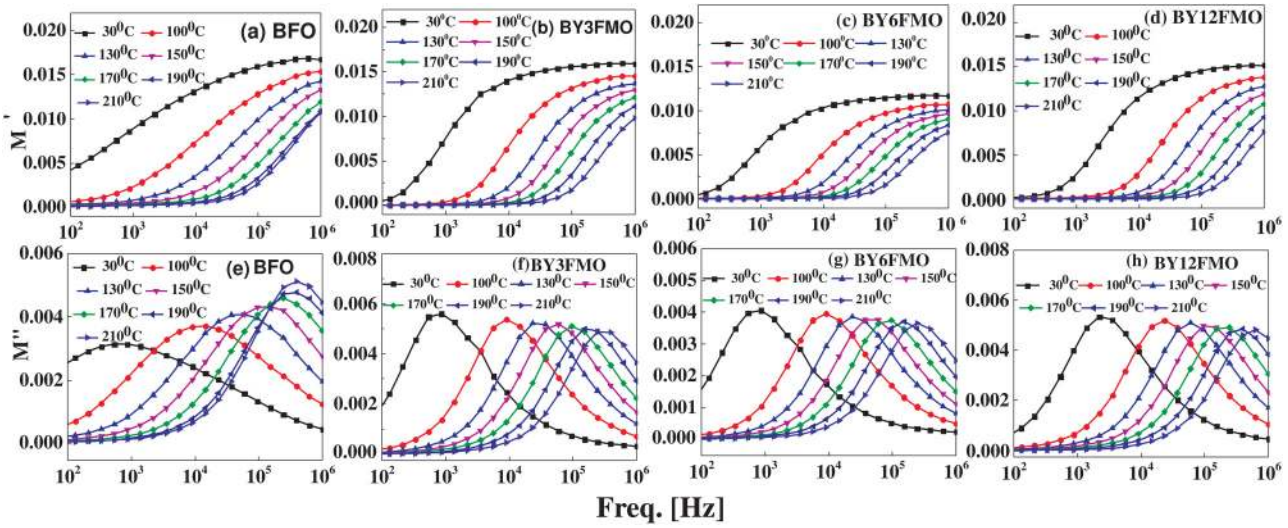

FIG. 10. Frequency dependence complex real (M′) modulus for (a) BFO, (b) BY3FMO, (c) BY6FMO, (d) BY12FMO, and imaginary (M″) modulus for (e) BFO, (f) BY3FMO, (g) BY6FMO, (h) BY12FMO at different temperatures.

in frequency. In each case for all samples, there exists a non-Debye type relaxation behavior and it shifts toward the higher frequency region with the increase in temperature confirming the relaxation being affected by thermal energy. The area below the maximum M″ is acting as a potential well, where the transport of charge carriers occurs from one region to another region with long-range hopping. Whereas the region outside the well hopping of charge carriers is short ranged.[38,39] The frequency (ω_{max}) corresponding to the maximum imaginary complex modulus (M_{max}) gives the most probable relaxation time (τ_{max}) for the charge carriers. The Arrhenius equation in terms of frequency can be expressed as

$$\omega_{max} = \omega_0 \exp\left(\frac{-E}{kT}\right), \tag{9}$$

where ω_0 and E are the exponential factor and activation energy, respectively. The activation energies of BFO, BY3FMO, BY6FMO, and BY12FMO can be calculated from the slope extracted from the plot between $\ln \omega_{max}$ and $\frac{1000}{T}$ (shown in Fig. 11). The evaluated activation energy of all compounds is given in Table IV. Generally, for a perovskite oxide material, the range of activation energy for singly ionized oxygen vacancy lies between 0.3 and 0.5 eV, whereas for doubly ionized oxygen vacancy, the range of activation energy lies between 0.6 and 1.2 eV.[40] Hence, in Y-Mn co-doped BFO system, the change in insulating behavior may be due to the double ionized oxygen vacancy.

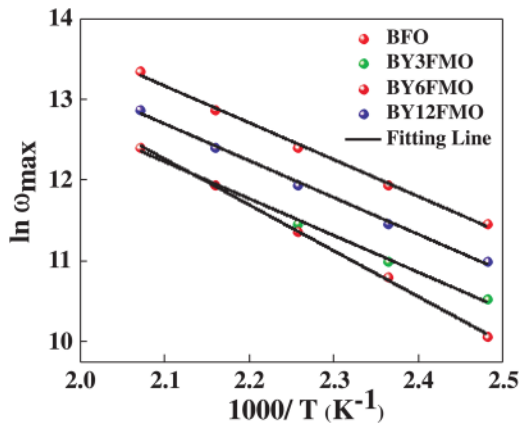

FIG. 11. The Arrhenius plot of $\ln \omega$ vs $\frac{1000}{T}$ for Y-Mn co-doped $Bi_{1-x}Y_xFe_{1-y}Mn_yO_3$ ($x = y = 0$; $x = 0.03, 0.06, 0.12$, $y = 0.05$).

VIII. AC CONDUCTIVITY ANALYSIS

The AC conductivity study is a useful approach to understand the response of materials to the external electric field and transport mechanism of charge carriers from BFO to Y-Mn co-doped BFO. Frequency variant AC conductivity at different temperatures for BFO, BY3FMO, BY6FMO, and BY12FMO is shown in Fig. 12. AC conductivity value depends on both dielectric constant (ϵ_r) and tangent loss ($\tan \delta$) from the relation

$$\sigma_{ac} = \epsilon_0 \epsilon_r \tan \delta. \tag{10}$$

From the figure it is clear that the AC conductivity value increases with increase in frequency due to faster movement of free charges with the externally applied field, whereas the magnitude of AC conductivity increases with increasing temperature at the low-frequency region and all of them merge to

TABLE IV. Activation energy extracted from the Arrhenius plots of $\ln \omega$ vs $\frac{1000}{T}$ and $\ln \sigma_{ac}$ vs $\frac{1000}{T}$ for Y-Mn co-doped $Bi_{1-x}Y_xFe_{1-y}Mn_yO_3$ ($x = y = 0$; $x = 0.03, 0.06, 0.12$, $y = 0.05$) samples.

		From $\ln \sigma_{ac}$ vs $\frac{1000}{T}$			
Sample code	From $\ln \omega$ vs $\frac{1000}{T}$	1 kHz	10 kHz	1000 kHz	1 MHz
BFO	0.69 ± 0.02	0.86	0.37	0.19	0.08
BY3FMO	0.75 ± 0.04	1.76	0.36	0.13	0.10
BY6FMO	0.83 ± 0.02	1.36	0.29	0.11	0.08
BY12FMO	0.90 ± 0.05	2.35	0.55	0.17	0.11

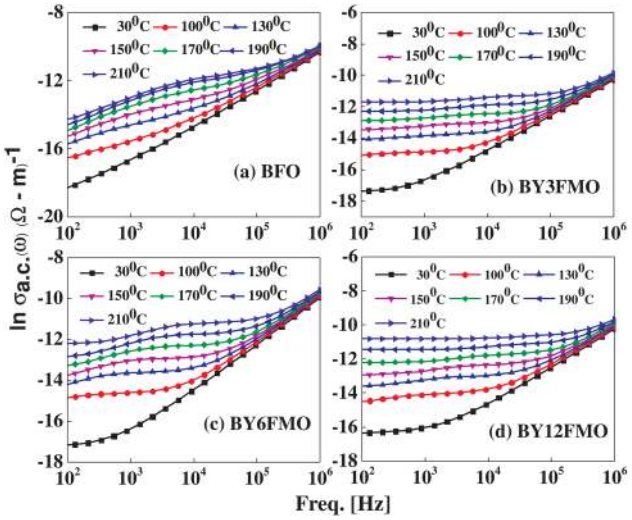

FIG. 12. Frequency dependent AC conductivity of BFO, BY3FMO, BY6FMO, and BY12FMO.

one point at the high-frequency region. The bandgap of BFO and Y-Mn co-doped BFO is in the range between 2.1 and 2.18 eV and behaves as an extrinsic semiconductor, where the movement of defect charges is faster with the increase in temperature resulting from the increase in conductivity.

It is also known that frequency dependence of AC conductivity obeys Jonscher's power law,[41]

$$\sigma_{ac} = \sigma_0 + A\omega^s = \sigma_0 + \sigma_\omega, \tag{11}$$

where σ_0 is the DC conductivity and "s" is an exponent. The σ_ω is explained on the basis of two mechanisms.

(i) In the first case, the value of "s" decreases with increase in temperature in correlated barrier hopping (CBH),[42] (ii) whereas in another case, the value of σ should be independent of temperature and small reduction should be observed with frequency in a quantum mechanical tunneling (QMT) through the barrier separated by two localized sites.[43]

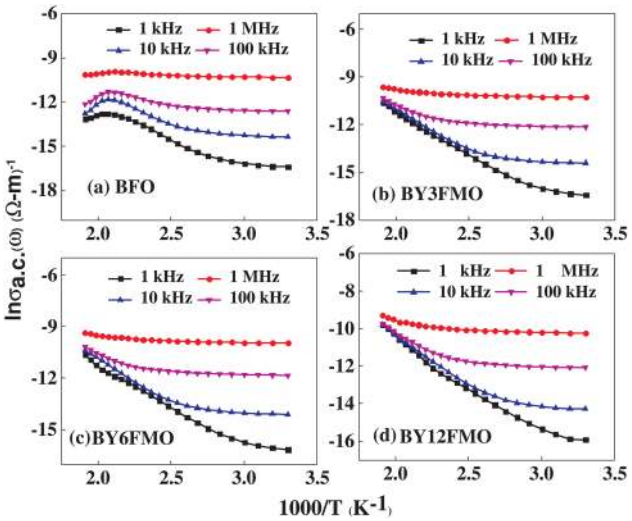

FIG. 13. The Arrhenius plots of $\ln \sigma_{ac}$ vs $\frac{1000}{T}$ for (a) BFO, (b) BY3FMO, (c) BY6FMO, and (d) BY12FMO.

In BFO and Y-Mn co-doped (BFO), the value of σ decreases with increase in temperature supporting CBH. Hence, additional ions such as Y^{3+} and Mn^{3+} in the Y-Mn co-doped BFO system provide good control of electrical behavior.

Figure 13 shows the Arrhenius plots of AC conductivity at different frequencies for BFO and Y-Mn co-doped system. The Arrhenius equation can be expressed as

$$\sigma_{a.c.} = \sigma_0 \exp\left(\frac{-E}{kT}\right), \tag{12}$$

where σ_0 is the electrical conductivity at infinite temperature. The activation energies are calculated for 1 kHz, 10 kHz, 100 kHz, and 1 MHz and are shown in Table IV. It is observed that the activation energy (E_a) decreases with increase in frequency confirming that E_a depends on frequency, which can be explained with conduction mechanism. Below 400 K, the AC conductivity was dependent only on frequency and it increases with increase in frequency due to the increase of hopping of charge carriers. Hence, the conduction mechanism is contributed by the long-range oxygen vacancies and the decrease in activation energy (E_a) could be expected with the increase in frequency.

IX. CONCLUSIONS

In summary, the un-doped and Y-Mn co-doped BFO ceramics are successfully prepared by the conventional solid state synthesis by using the high energy ball milling technique. X-ray study confirms that all the samples are restricted in the Rhombohedral (R3c: space group) structure. More information regarding structural distortion after co-doping is obtained from Raman spectroscopy. Reduction in the average grain size is confirmed from FESEM micrographs. The saturated and enhanced ferromagnetic behavior is observed from magnetic measurements. Frequency dependent dielectric, impedance, complex, electrical modulus are studied to establish the relaxation behavior involved in the Y-Mn co-doped system and the contribution to electrical properties from grain and grain boundaries. As the material is showing good dielectric properties with Y-Mn co-doping, there is a good possibility of exploring dielectric applications using this material.

ACKNOWLEDGMENTS

A. K. Jena acknowledges IIT Hyderabad for providing research facility and Council of Scientific and Industrial Research (CSIR) for providing financial support. The authors acknowledge the support of Dr. J. Arout Chelvane from DMRL, Hyderabad for magnetic measurements.

[1]W. Eerenstein, N. D. Mathur, and J. F. Scott, Nature **442**, 759 (2006).
[2]R. Ramesh and N. A. Spaldin, Nat. Mater. **6**, 21 (2007).
[3]M. Gajek, M. Bibes, S. Fusil, K. Bouzehouane, J. Fontcubert, A. Barthelemy, and A. Fert, Nat. Mater. **6**, 296 (2007).
[4]Y. Tokura, Science **312**, 1481 (2006).
[5]G. Catalan and J. F. Scholl, Adv. Mater. **21**, 2463 (2009).
[6]V. Goian, S. Kamba, S. Greicius, D. Nuzhnyy, S. Karimi, and I. M. Reaney, J. Appl. Phys. **110**, 074112 (2011).
[7]A. Nagesetti, A. Rodzinski, E. Stimphil, T. Stewart, C. Khanal, P. Wang, R. Guduru, P. Liang, I. Agoulnik, J. Horstmyer, and S. Khizroev, Sci. Rep. **7**, 1610 (2017).

[8]G. L. Song, Y. C. Song, J. Su, X. H. Song, N. Zhang, T. X. Wang, and F. G. Chang, J. Alloys Comp. **696**, 503–509 (2017).
[9]T. Durga Rao, R. Ranjith, and S. Asthana, J. Appl. Phys. **115**, 124110 (2014).
[10]S. Pattnayak, R. N. P. Choudhary, S. R. Shannigrahi, P. R. Das, and R. Pahee, J. Magn. Magn. Mater. **341**, 158–164 (2013).
[11]S. Chauhan, M. Kumar, S. Chhoker, S. C. Katyal, H. Singh, M. Jewariya, and K. L. Yadav, Solid State Commun. **152**, 525–529 (2012).
[12]Y.-S. Chiang, C.-S. Tu, P.-Y. Chen, C.-S. Chen, J. Anthoniappen, Y. Ting, T.-S. Chan, and V. H. Schmidt, Ceram. Int. **42**(11), 13104–13112 (2016).
[13]C. A. Wang, H. Z. Pang, A. H. Zhang, X. B. Lu, X. S. Gao, M. Zeng, and J.-M. Liu, Mater. Res. Bull. **70**, 595–599 (2015).
[14]A. K. Jena, J. A Chelvane, and J. Mohanty, AIP Conf. Proc. **1953**(1), 120072 (2018).
[15]T. Durga Rao and S. Asthana, J. Appl. Phys. **116**, 164102 (2014).
[16]J. Xu, D. Xie, C. Yin, T. Feng, X. Zhang, G. Li, H. Zhao, Y. Zhao, S. Ma, T.-L. Ren, Y. Guan, X. Gao, and Y. Zhao, J. Appl. Phys. **114**, 154103 (2013).
[17]A. K. Jena and J. Mohanty, J. Mater. Sci. Mater. Electron. **29**, 5150–5156 (2017).
[18]I. Sosnowska, T. Peterlin-Neumaier, and E. Steichele, J. Phys. C **15**, 4835 (1982).
[19]C. A. Scurti, N. Auvray, M. W. Lufaso, S. Takeda, H. Kohno, and D. J. Arenas, AIP Adv. **4**, 087125 (2014).
[20]M. K. Singh, H. M. Jang, S. Ryu, and M. H. Jo, Appl. Phys. Lett. **88**, 042907 (2006).
[21]H. Fukumura, H. Harima, K. Kisoda, M. Tamada, Y. Noguchi, and M. Miyayama, J. Magn. Magn. Mater. **310**, 367 (2007).
[22]G. L. Yuan, S. W. Or, and H. L. W. Chan, J. Appl. Phys. **101**, 064101 (2007).
[23]Z. Quan, W. Liu, H. Hu, S. Xu, B. Sebo, G. Fang, M. Li, and X. Z. Zhao, J. Appl. Phys. **104**, 084106 (2008).
[24]A. A. Porporati, K. Tsuji, M. Valant, A.-K. Axelssond, and G. Pezzotti, J. Raman Spectrosc. **41**, 84–87 (2010).
[25]Y. Lin, P. Kang, H. Yang, G. Zhang, and Z. Gou, Power Technol. **284**, 143–148 (2015).
[26]C. F. Chung, J. P. Lin, and J. M. Wu, Appl. Phys. Lett. **88**, 242909 (2006).
[27]N. Shamir, E. Gurewitz, and H. Shaked, Acta Cryst. **34**, 662–666 (1978).
[28]X. Wen, Z. Chen, E. Liu, X. Lin, and C. Chen, J. Alloys Comp. **678**, 511–517 (2016).
[29]D. Kothary, V. Raghavendra Reddy, A. Gupta, V. Sathe, A. Banerjee, S. M. Gupta, and A. M. Awasthi, Appl. Phys. Lett. **91**, 202505 (2007).
[30]J. C. Maxwell, *A treatise on electricity and magnetism* (Clarendon Press, Chelsea, Oxford, 1973), Vol. 1.
[31]D. K. Mahato, A. Dutta, and T. P. Sinha, Phys. B Condens. Matter **406**, 2703 (2011).
[32]P. Tirupathi, N. Kumar, M. Pastor, A. C. Pandey, and R. N. P. Choudhary, J. Appl. Phys. **117**, 074105 (2015).
[33]J. liu, C. G. Duan, W. G. Yin, W. N. Mei, R. W. Smith, and J. R. Hardy, Phys. Rev. B **70**, 144106 (2004).
[34]B. Tiwari and R. N. P. Choudhary, J. Alloys Comp. **493**, 1–10 (2010).
[35]A. R. West, D. C. Sinclair, and N. Hirose, J. Electroceram. **1**, 65 (1997).
[36]J. R. Macdonald, *Impedance Spectroscopy* (John Wiley and Sons, New York, 1987), Chap. 4.
[37]M. Sural and A. Ghosh, J. Phys. Condes. Matter **10**, 10577 (1998).
[38]P. Pandit, S. Satapathy, and P. K. Gupta, Physica B **406**, 2669 (2011).
[39]S. F. Shao, J. L. Zhang, P Zheng, W. L. Zhong, and C. L. Wang, J. Appl. Phys. **99**, 084106 (2006).
[40]S. Sarangi, T. Badapanda, B. Behera, and S. Anwar, J. Mater. Sci. Mater. Electron. **24**, 4033 (2013).
[41]A. K. Jonscher, Nature **267**, 673 (1977).
[42]G. E. Pike, Phys. Rev. B **6**, 1572 (1972).
[43]A. Ghosh, Phys. Rev. B **47**, 15537 (1993).